



A method for the identification of hydraulic damper characteristics from steady velocity inputs

Branislav Titurus^{a,*}, Jonathan du Bois^a, Nick Lieven^a, Robert Hansford^b

^a Department of Aerospace Engineering, University of Bristol, Queens Building, University Walk, Bristol BS8 1 TR, UK

^b Box 267, Westland Helicopters, Lysander Road, Yeovil, Somerset, UK

ARTICLE INFO

Article history:

Received 15 October 2009

Received in revised form

18 May 2010

Accepted 27 May 2010

Available online 2 June 2010

Keywords:

Hydraulic damper

Experimental characterisation

Triangular excitation

ABSTRACT

The research presented in this paper investigates the possibility of precise experimental identification of steady damper characteristics. The paper considers velocity sensitive and nominally symmetric hydraulic dampers. The proposed identification methodology is based on a piecewise constant velocity excitation. One goal of the paper is to analyze the transient nature of the damper response in the context of finite permissible piston displacements and first order transient effects due to elastic elements in the damper structure. The proposed methodology is formalized in a framework suitable for experimental design, allowing the detailed study of steady state damper performance. The second goal of the paper is to demonstrate the practical application of the proposed methodology. It is applied to the case of a safety critical hydraulic damper used for stability augmentation in production helicopters. The research work presented shows that this methodology can be used for identification in a finite but relatively wide range of piston velocities. The case study demonstrates a successful example of damper property identification where the resulting characteristics prove useful as a tool for model validation. Finally, the identification results are related to the results of a more traditional test with harmonic piston excitation.

© 2010 Elsevier Ltd. All rights reserved.

1. Introduction

It is shown in the published literature, for example [1–3], that complex fluid dynamics phenomena occurring in hydraulic dampers can be, in the low frequency range (from 0 to 30 Hz according to Duym [4] and Yung and Cole [5]), efficiently modelled on the basis of hydraulic system theory, described in Ref. [6]. This theory addresses first order dynamic effects observed particularly in the damper velocity-force characteristics in the form of the “hysteretic” loops. These loops are manifestations of the internal dynamic relationships and the physical effects occurring typically in high-pressure hydraulic systems, [7,8], which include fluid compressibility [6], fluid inertial effects [9] and other dynamic effects. Hydraulic system theory can accommodate these effects during the modelling process and it has traditionally been used in the damper and hydraulic actuator modelling communities for the last few decades, [1,10]. Moreover, this theory is amenable to other physical domains such as mechanical [11] and thermal domains [12]. Also, it is often used in the context of multi-disciplinary [13] and mechatronic studies [14].

Important elements in hydraulic system modelling are steady state models of the flow transporting or restricting elements such as pipes, valves, orifices or leakage paths. Characterisation of these elements was a traditional field of

* Corresponding author. Tel.: +44 117 3315552; fax: +44 117 9272771.

E-mail address: Brano.Titurus@bristol.ac.uk (B. Titurus).

Nomenclature

A_O	cross-sectional area of the orifice	Q	volumetric flow rate
A_P	cross-sectional area of the symmetric piston	Q_j	flow rate through j th flow path
B	constant isothermal bulk modulus of a hydraulic fluid	$Q_{j,k}$	flow rate through k th pressure reducing segment located in j th flow path
B_{eff}	effective bulk modulus	Q_β, Q_N, Q_P	flow rates due to fluid compressibility, flow transfer and piston displacement
B_G	gas or air bulk modulus	$R(d)$	function of normalised piston stroke and piston starting position
C_α	coefficient of the general exponential pressure-flow model	T	time interval
C_D	discharge coefficient	T^\pm	positive and negative slope half-periods for the time interval T
c_i	coefficient of the general polynomial pressure-flow model	T_{max}, T_{lim}	maximum test time and limit test time for the damper piston travel
c_1, c_2	coefficient of the laminar and turbulent pressure-flow models	T_R	relaxation time
D_L, D_Q	coefficient of the linear and quadratic force-velocity damper model	t	physical time
d	normalised piston stroke	V	lumped volume of the hydraulic fluid
d_C	mean diameter of the damper cylinder	V_C, V_G	volume of the container and the total volume of the gas or air entrapped in the container
E	Young's modulus of the damper cylinder material	$V_{0,i}, V_i$	initial and variable volume of i th hydraulic chamber
F_D	damper force	\mathcal{V}	composite volume function
\bar{F}_D^\pm	identified steady level of the overall damper force	W_P	constant piston velocity
$F_{D,h}$	hydraulic component of the damper force	Y_P	amplitude of the triangular piston excitation
F_f	friction force	$y_P, \dot{y}_P, \ddot{y}_P$	piston displacement, velocity and acceleration
f^{-1}	inverse function to function f	α	exponent in the exponential pressure-flow model
G_1, G_2, G_3	laminar, turbulent and laminar-turbulent pressure differential convergence coefficients	β	fluid compressibility factor related to the fluid bulk modulus, $\beta = 1/B$
h_C	wall thickness of the damper cylinder	$\beta_{0,F}, \beta_{eff}$	nominal and effective fluid compressibility
K_1, K_2	coefficients of the damper model representing Maxwell viscoelastic unit	Δp	pressure difference between two damper chambers
k_C, k_P	stiffnesses of the cylinder and piston damper attachment points	Δp_j	pressure difference in j th flow path
k_i	i th exponent in the polynomial pressure-flow model	$\Delta p_{j,k}$	increment in the pressure difference in j th flow path due to k th pressure reducing segment
l_O	orifice pipe length	μ	dynamic fluid viscosity
m_P	mass of the damper piston	ρ	density of hydraulic fluid
N_F	number of flow paths between the damper chambers	ϕ	normalised pressure difference
N_j	number of pressure reducing segments in j th flow path	$\varphi(\Delta p)$	adjusted measure of the pressure difference
N_S	number of polynomial terms in the polynomial pressure-flow model	φ_P	phase of the triangular piston displacement excitation
N_V	number of test points	Ω	angular frequency of triangular piston excitation
p, \mathcal{P}	absolute and homogeneous pressure	$\mathcal{E}(\odot)$	auxiliary function for the triangular waveform generation
p_i	pressure in i th damper fluid chamber	tri(\odot)	function generating the triangular waveform
		\odot	absolute value

experimental hydraulic studies [15,16], and recently also computational fluid dynamics investigations (e.g. [17]). Another important element in hydraulic system modelling describes the transient or dynamic effects in hydraulic systems, for instance those caused by fluid compressibility and other elastic effects [6]. The combination of the two basic elements mentioned is usually used along with the laws of conservation to provide system dynamic equations, with pressures frequently representing the dynamic states (for example Refs. [2,3,9–11]).

The goal of this paper is to evaluate a framework for experimental characterisation of damper behaviour. The approach adopted here focuses on the characterisation of velocity-sensitive hydraulic dampers. Semi-empirical characterisation of the components is known to be used in hydraulic system modelling. For example, Ferreira et al. [18] applied this approach in the case of static and dynamic servo-valve modelling and Hayashi et al. [19] used an experimentally determined and parameterised representation of the relief valve discharge coefficient. In the current paper, a similar approach is used to address the problem of damper modelling.

The three physical effects that tend to interact during standard damper tests are the elastic effects in the damper (e.g. fluid compressibility), the hydraulic resistance, and to some extent also mechanical friction between moving damper parts. The primary interest of the research presented in this paper is the isolation of the steady state damper responses from their transients. Historically, the two approaches used to identify such results are: (a) a “filtering” approach and (b) a steady component excitation. The “filtering” approach was originally applied by Duym [4] and it was used recently by Yung and Cole [5]. This approach tries to identify a subset of the experimental data that is least affected by compressibility and other dynamic effects, while assuming standard test conditions. If prescribed test conditions can be applied, the alternative approach uses a form of the excitation that attempts to establish steady flow conditions in the damper. In the case of velocity-sensitive devices this is constant velocity excitation.

Constant velocity excitation, or *iso-kinetic* excitation, is a natural choice to consider in damper investigations. The concept of the constant-velocity excitation and its application in damper characterisation was investigated by Basso [20] and Basso and Fanti [21]. The work summarised in [20] introduced the general concept and applied it within the framework of displacement–velocity force maps, characterising the global performance of dampers. The methodology was applied in [21] for the identification of displacement–velocity force maps of two devices: a shock absorber and a mountain bike front fork. Both works, [20,21], primarily focused on experimental issues, instrumentation and identification the context of displacement–velocity force maps [22].

The focus of the current work is on the formalisation of the constant velocity excitation methodology, and the demonstration of its use on an industrially applied device. The original motivation to employ constant velocity excitation comes from a specific experimental damper configuration with strong interaction between the transient and the steady state fluid flow effects, described in Ref. [23]. High flow resistance of the primary flow path required special treatment to allow identification and validation of the damper model. This paper addresses the problem of the response unsteadiness under the realistic conditions of non-zero effective fluid compressibility and finite volume in the tested dampers. Furthermore, the methodology and mutual relationship between the test factors are formulated within the scope of the test signal’s amplitude-period envelope, visualised by means of a logarithmic chart. This representation allows the formal design of experiments in the context of the relevant constraints. A demonstration of this approach is performed on a lag damper, used for stability purposes in helicopter rotors.

The organisation of the remainder of this paper is as follows: Section 2 provides a theoretical basis for the experimental considerations. Section 3 represents the central part of this paper. It proposes the experimental procedure, provides a basis for evaluation of the response unsteadiness, and summarises the experimental factors in the test design. Section 4 demonstrates the use of the proposed method on the industrial damper. The conclusions are presented in Section 5.

2. General theoretical considerations

2.1. Damper model

The damper design considered in this paper is a hydraulic damper with symmetric piston and two working chambers. A number of functional flow paths can be identified between these chambers. Forced movement of the piston located in the damper cylinder induces fluid flow between the chambers through these flow paths. This process is accompanied by energy transformation, particularly to heat, such that the damper acts as an energy dissipating element within the overall system or structure. The process of energy transformation is manifested in the form of pressure losses in the fluid continuum as the fluid is forced to flow across the flow restricting elements and paths. The functional manifestation of these losses is the force with which the damper resists the piston movement. The model configuration is shown in Fig. 1.

Assuming this damper organisation, the damper model can be represented by a non-linear, non-autonomous ordinary differential equation, as derived in [24], and it is this model that will be used in the current work. The system has a single dynamic state: the pressure difference between two working chambers, denoted $\Delta p = p_1 - p_2$, where p_1 and p_2 are the absolute pressures in the chambers of the damper. It is assumed that these chambers can be modelled as lumped variable

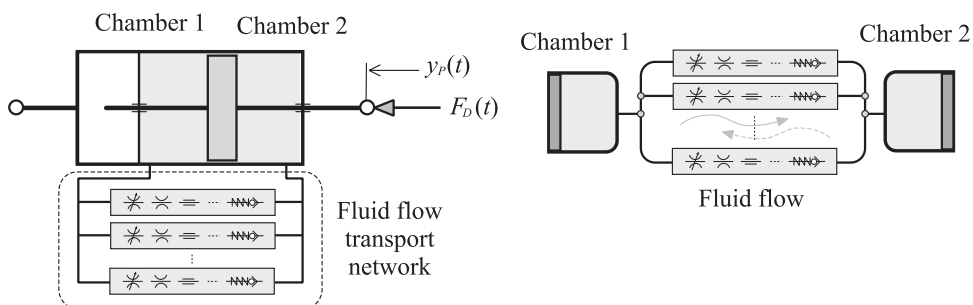


Fig. 1. General organisation of the two-chamber symmetric hydraulic damper.

fluid volumes with compressible fluid. It is also assumed that the fluid behaviour can be characterised by the constant parameters of the fluid density ρ , dynamic viscosity μ and bulk modulus B , where this parameter is related to the fluid compressibility $\beta=1/B$. Both the model of the damper and the later experimental investigations assume isothermal operational conditions. The definition of the bulk modulus [6] in the form $B=-V(dp/dV)$, where V is the fluid volume with internal pressure p , allows construction of the equation of the pressure changes in this volume. Using the bulk modulus definition, this equation adopts the form $\dot{p} = -(B/V)\dot{V}$, where \dot{V} can be seen as the total volumetric flow rate in the container including variable volume effects, fluid inflows and fluid outflows. Using this equation for both damper chambers along with the condition $\Delta\dot{p} = \dot{p}_1 - \dot{p}_2$ enables formulation of a single damper state equation. For the damper with two chambers, symmetric piston and N_F flow paths, the following model can be written [24]:

$$\Delta\dot{p} = B_{eff} \left(\frac{1}{V_1(y_p)} + \frac{1}{V_2(y_p)} \right) \left[A_p \dot{y}_p - \sum_{j=1}^{N_F} Q_j(\Delta p) \right] \tag{1}$$

where A_p is the (symmetric) piston cross-sectional area, y_p and \dot{y}_p are the piston displacement and velocity, respectively, Q_j is the volumetric flow rate through the j th flow path, B_{eff} is the effective constant bulk modulus of the working fluid, V_1 and V_2 are the variable volumes of the two damper chambers and $\Delta\dot{p}$ denotes the time derivative of the state Δp .

Eq. (1) can be adjusted to a form which represents a volumetric equilibrium of the flow rates

$$\beta_{eff} \mathcal{V}(y_p) \Delta\dot{p} + \sum_{j=1}^{N_F} Q_j(\Delta p) = A_p \dot{y}_p$$

$$\mathcal{V}(y_p) = V_1 V_2 / (V_1 + V_2), V_1(y_p) = V_{0,1} - A_p y_p, \quad V_2(y_p) = V_{0,2} + A_p y_p \tag{2}$$

where $V_{0,1}$ and $V_{0,2}$ are the initial volumes of the chambers and $Q_p = A_p \dot{y}_p$ represents the flow rate induced by the movement of the piston; the latter is comprised of the demanded flow rate, $Q_N = \sum_{j=1}^{N_F} Q_j(\Delta p)$, representing the total flow rate through the available “hydraulic paths” that are located between the damper chambers, and the induced flow rate, $Q_\beta = \beta_{eff} \mathcal{V}(y_p) \Delta\dot{p}$, representing an apparent flow rate due to effective fluid compressibility: $\beta_{eff}=1/B_{eff}$. This notation allows interpretation of Eq. (2) as an equation of the volumetric flow rate equilibrium, $Q_\beta + Q_N = Q_p$.

Supplementing Eq. (2) with the further assumption of incompressibility, i.e. $\beta_{eff}=0$, leads to $Q_\beta=0$, and. $Q_N=Q_p$. It is the term Q_β , however, that introduces the dynamic features into the behaviour of the hydraulic damper model in Eq. (1). When in use, this is manifested by delayed and smoothed damper responses with respect to the responses generated by an equivalent damper with zero or reduced compressibility. The use of *effective* compressibility reflects the fact that in real conditions the inherent fluid compressibility combines with other similar effects. One possible formulation of this quantity is as follows:

$$\beta_{eff} = \frac{1}{B_{eff}} = \sum_{(i)} \beta_i \approx \beta_{0,F} + \frac{1}{(h_C/d_C)E} + \frac{1}{(V_C/V_G)B_G} + A_p^2 \left(\frac{1}{V_1} + \frac{1}{V_2} \right) \left(\frac{1}{k_C} + \frac{1}{k_p} \right) \tag{3}$$

where $\beta_{0,F}$ is the nominal constant fluid compressibility factor, h_C , d_C and E are the wall thickness, mean diameter and Young’s modulus, respectively, of the damper cylinder assuming an approximate theory of thin-walled pressure vessels [6], V_C , V_G and B_G are the total volume of the container, the total volume of the gas or air entrapped in the container and the gas or air bulk modulus [6], respectively, and k_C and k_p are the equivalent stiffnesses of the attachment fixture on the side of the cylinder and the piston, respectively.

The second and third terms on the right hand side of Eq. (3) are derived by Merritt [6]. The second term introduces the effect of finite cylinder stiffness, where the cylinder is represented as a thin-walled internally pressurised vessel. The third term represents the volumetric effect of entrained air or gas. Merritt [6] illustrated these effects on an example where 1% of entrained air in a steel pipe with $d_C=6h_C$ causes $\beta_{eff} \approx 4\beta_{0,F}$. The fourth term, introduced here, represents the effects of finite stiffness in the damper attachment fixtures. This term is derived while assuming a serial arrangement of the damper with two linear “springs”, of stiffness k_C and k_p , respectively. Within the context of this approach, the velocity term \dot{y}_p represents the relative velocity between ends of these springs, i.e. the springs are considered to be an integral part of the damper. The reduction in these stiffnesses causes an increase in the associated compressibility term, leading to direct increase in β_{eff} .

2.2. Pressure-flow relationships for damper model

The nature of the term Q_N determines the global behaviour of the dampers. It represents the inherent static characteristics of the flow transport paths under steady flow conditions and the term Q_j represents the static characteristics of the j th individual flow path. Furthermore, the j th path can be seen as an independent fluid flow route consisting of N_j segments causing energy losses. Each segment in the j th path participates in the overall pressure loss $\Delta p \equiv \Delta p_j$, such that $\Delta p_j = \sum_{k=1}^{N_j} \Delta p_{j,k}$. Dependency between the upstream–downstream pressure differential and the volumetric flow rate forms the static pressure–flow characteristics, i.e. $Q_j(\Delta p)$ or $Q_{j,k}(\Delta p_{j,k})$. Assuming incompressible flow, the direct and the inverse characteristics of the j th path are

$$\Delta p = f_j(Q_j) \rightarrow Q_j = f_j^{-1}(\Delta p) \tag{4}$$

One parametric family of these static models is based on the general exponential form

$$\Delta p = \text{sign}(Q_j) C_\alpha |Q_j|^\alpha, \quad \alpha \in [0, \alpha_{\max}] \quad (5)$$

where $\text{sign}(\odot)$ is the sign function, C_α is the coefficient of the exponential model and α is a specific coefficient of the model, usually specified such that $\alpha_{\max} \leq 2$.

The model in Eq. (5) is used to represent different fluid flow modes, such as developed laminar flow, with $\alpha=1$ [2,25], turbulent flow, with $\alpha=2$ [2,3,6,9], or a flow model based on the Blasius formula for mixed flow in straight pipes, with $\alpha=1.75$ [4,26]. Model (5) is related to the rational polynomial formulation [26]

$$\Delta p = \sum_{i=1}^{N_s} c_i Q_j^{k_i} \quad (6)$$

where N_s is the number of polynomial terms, exponent $k_i \in [0,2]$ and the parameter c_i depends on the flow character, geometry and other relevant factors. Solving model (6) for Q_j , for a given Δp , allows its use in Eqs. (1) or (2). A special case of model (6) comes with $N_s=2$, $k_1=1$ and $k_2=2$. Solving this model for Q_j provides an explicit laminar-turbulent flow model representing two discrete pressure loss segments in series inducing laminar followed by turbulent pressure losses [22,25],

$$\begin{aligned} \Delta p &= c_1 Q_j + c_2 Q_j |Q_j| \\ Q_j &= \text{sign}(\Delta p) (-c_1 + \sqrt{c_1^2 + 4c_2 |\Delta p|}) / (2c_2) \end{aligned} \quad (7)$$

where c_1 corresponds to the laminar loss model and c_2 is related to the turbulent losses. If $c_1=0$, then $Q_j \equiv Q_{j,q} = \text{sign}(\Delta p) \sqrt{|\Delta p|/c_2}$ and conversely, for $c_2=0$ the flow rate is $Q_{j,l} = \Delta p/c_1$. The previous models, given in Eqs. (5)–(7), can be related to specific fluid, geometry and other context dependent parameters. In the case of fully developed laminar flow in a smooth pipe the relationship between the pressure and the flow has the following form: $\Delta p = c_1 Q_j$ [6], where $c_1 = 8\pi\mu l_0/A_0^2$, μ is the dynamic fluid viscosity, and l_0 and A_0 are the length and the cross-sectional area of the pipe, respectively. In the case of turbulent flow through a flow restrictor the relationship between the pressure and the flow has the form $\Delta p = c_2 Q_j |Q_j|$, where $c_2 = \rho / (2C_D^2 A_0^2)$, ρ is the density of the fluid and C_D is the discharge coefficient [6].

Alternative parametric representations exist for describing the physical aspects of the complete individual flow paths, or for the separate discrete flow restricting elements, and the choice of model depends on the user's interpretation of the problem, the internal organisation of the flow paths, and personal preferences. One objective of this paper is to evaluate an experimental method that can be used for direct identification of the pressure–flow relationship, or as a decision making support tool during the modelling process. The pressure–flow model used within this paper for analytical studies will be based on the model in Eq. (7).

2.3. A note on induced damper forces

Assuming known initial conditions (e.g. $\Delta p(0)=0$) and external excitation $y_p(t)$, integration of Eq. (1) or (2) can be used to predict damper behaviour. Often, the following model can be used to compute the forces induced by the damper

$$F_D(t) = A_p \Delta p + m_p \ddot{y}_p + F_f \quad (8)$$

where m_p is the mass of the piston and F_f represents the friction effects between the moving damper parts. The hydraulic component of the damper force $F_{D,h} = A_p \Delta p$ in Eq. (8) is often used as the only damper force representative, i.e. $F_D \approx F_{D,h}$, as these devices are usually designed to induce the forces that are primarily determined and dominated by their internal hydraulic configuration.

Multiplying Eq. (2) by A_p provides a new form of the hydraulic model, with $F_{D,h}$ as the state variable

$$\begin{aligned} \beta_{\text{eff}} \mathcal{V}(t) \dot{F}_{D,h} + H_N(F_{D,h}) &= A_p^2 \dot{y}_p \\ H_N(F_{D,h}) &= A_p Q_N(F_{D,h}/A_p) \end{aligned} \quad (9)$$

This form of damper model gives closer information about the link between the flow restricting features in the damper, the first order dynamics (due to the assumption of a compressible fluid) and the force with which the damper acts against the imposed piston motion.

The following example assumes a single flow path, $Q_N = Q_j$, with one laminar pressure loss segment, $Q_j = (1/c_1) \Delta p$. Substitution of these relationships into Eq. (9) gives the following model:

$$\beta_{\text{eff}} \mathcal{V}(t) \dot{F}_{D,h} + c_1^{-1} F_{D,h} = A_p^2 \dot{y}_p \quad (10)$$

Furthermore, when assuming small prescribed oscillations $y_p(t)$ around the central position, such that $V_{0,2} = V_{0,1}$, $y_p \ll V_{0,1}/A_p$ and $\mathcal{V}(t) \approx V_{0,1}/2$, model (10) can be written in the following linear form:

$$\begin{aligned} \dot{F}_{D,h} + K_1 F_{D,h} &= K_2 \dot{y}_p \\ K_1 &= (2\beta_{\text{eff}})/(c_1 V_{0,1}), \quad K_2 = 2A_p^2 \beta_{\text{eff}}/V_{0,1} \end{aligned} \quad (11)$$

Model (11) can be related to the model of the Maxwell viscoelastic unit [2,27], which can be represented as a series arrangement of a linear spring and a dashpot element [27]. Due to the simplicity of this model, it can serve as an illustration of the effects provided by the different model components and the different physical parameters.

The parameters of the damper’s response such as the relaxation time due to step input, i.e. $\dot{y}_p = W_p = \text{const}$ for $t \geq t_0$, and the value of the steady state response can be defined. The relaxation time is defined as $T_R = 1/K_1 = c_1 \beta_{\text{eff}} V_{0,1}/2$ and the steady response of system (11) is $\bar{F}_{D,h} = (K_2/K_1)W_p = c_1 A_p^2 W_p$. These two relationships reveal some facts about the nature of the damper response during and after the transition between two constant velocities $W_{p,1}$ and $W_{p,2}$, for example $W_{p,2} = -W_{p,1}$. The value of T_R depends on β_{eff} and therefore it affects the transition to the steady force values. These in turn, after scaling by A_p , lead to the pressure-flow relationship $\Delta \bar{p} = c_1 Q_{p,W}$. Considering Eq. (3), in any practical situation the parameter β_{eff} will be seriously affected by the presence of elastic damper components, most significantly the air or gas trapped in the hydraulic system [6,8].

The previous paragraph provides a description of the behaviour of the damper for the selected set of assumptions. In relation to Eq. (9), in practical circumstances, the nature of H_N can be uncertain. Furthermore, some other effects will be unavoidably present in the measured signals, for example the friction component, F_f . Despite these unwanted contributions, the data acquired from the test using step changes in the velocity can provide useful information for analytical work with the damper models. Importantly, however, the dynamic term $Q_\beta = \beta_{\text{eff}} \mathcal{V}(y_p) \Delta \dot{p}$ from Section 2.1 is unsteady during the whole range of the piston motion. Even with the justifiable assumption of constant fluid compressibility β_{eff} , the function \mathcal{V} is not constant and its range is $\mathcal{V}(y_p) \in [0, (V_{0,1} + V_{0,2})/4]$, assuming the case of a damper without any “dead” volumes.

3. Formulation and analysis of the test methodology

3.1. Damper model for steady test conditions

The rationale behind the proposed testing methodology is the need for a systematic investigation of the performance of the damper, using specific test conditions to promote the investigation of only a selected subset of its physical behaviours. In this instance, the tests are designed to induce steady operational conditions by suppressing or cancelling the dynamical aspects of the damper behaviour. In accordance with the assumed models, Eqs. (1) or (2), this situation is achieved through the use of constant excitation: $A_p \dot{y}_p = \text{const}$. The implication of this choice, in an ideal analytical setting, is that $\dot{y}_p = W_p \in \mathbb{R}$, $y_p = W_p t$ and $\ddot{y}_p = 0$. Assuming this form of excitation, model (2) can be written in the following form:

$$\begin{aligned} \beta_{\text{eff}} \mathcal{V}(t) \Delta \dot{p} + Q_N(\Delta p) &= A_p W_p, \\ \mathcal{V} &= V_1 V_2 / (V_1 + V_2), \quad V_1(y_p) = V_{0,1} - A_p W_p t, \quad V_2(y_p) = V_{0,2} + A_p W_p t. \end{aligned} \tag{12}$$

A constraint is applied for the maximum time and travel, $t \in [0, T_{\text{max},i}]$, where $T_{\text{max},i} < T_{\text{lim},i}$, and $T_{\text{lim},i} = V_{0,i} / (A_p W_p)$, $i=1,2$ represents the maximum possible time for the travel due to physical damper dimensions. The limiting case in this model is achieved when $|y_p| \rightarrow V_{0,i} / A_p$, $i=1,2$, i.e. when $V_i(y_p) \rightarrow 0$ and $t \rightarrow V_{0,i} / A_p W_p$. Accordingly, the time can be normalised to give $d = t / (V_{0,i} / A_p W_p)$, which is also effectively a normalised measure of the piston stroke.

The model given in Eq. (12) represents a non-linear differential equation with time-variable coefficient and the constant excitation term $A_p W_p$ assumed to be applied at $t=0$. Initial conditions of this problem are assumed to be $\Delta p(0) = 0$, i.e. $p_1 = p_2$. The general integral of the problem can then be determined from the following differential form:

$$\frac{d(\Delta p)}{A_p W_p - Q_N(\Delta p)} = \frac{dt}{\beta_{\text{eff}} \mathcal{V}(t)} \tag{13}$$

Integration of this general problem leads to the following integral equation:

$$\int_0^{\Delta p} \frac{dP}{A_p W_p - Q_N(P)} = \ln \left(\left(\frac{V_{0,1}}{V_{0,2}} \right) \left(\frac{V_{0,2} + A_p W_p t}{V_{0,1} - A_p W_p t} \right) \right)^{B_{\text{eff}} / A_p W_p} \tag{14}$$

Further integration of model (14) depends on the specific pressure-flow model Q_N .

3.2. Theoretical analysis of test configuration

So far it has been assumed that the pressure differential converges on a steady state under constant velocity excitation. In this section, the validity of that assumption is investigated. The damper symmetry allows consideration of only a positive piston velocity, $W_p > 0$, and application of the normalised piston stroke $d = t / (V_{0,1} / A_p W_p)$ to Eq. (14) gives

$$\begin{aligned} \int_0^{\Delta p} \frac{dP}{A_p W_p - Q_N(P)} &= \ln R(d)^{-B_{\text{eff}} / A_p W_p} \\ R(d) &= \frac{1-d}{1+(V_{0,1}/V_{0,2})d} \end{aligned} \tag{15}$$

For the pressure-flow model, the case of a serial linear-quadratic restriction as described by Eq. (7) is assumed so that

$$\int_0^{\Delta p} \frac{2c_2}{2A_p W_p c_2 - \text{sign}(P)(-c_1 + \sqrt{c_1^2 + 4c_2|P|})} dP = \ln R(d)^{-B_{\text{eff}} / A_p W_p} \tag{16}$$

Integrating the previous equation for positive W_p and thus positive Δp , the pressure differential is defined as follows:

$$\Delta p = \frac{1}{4c_2} \left[\left\{ 2A_p W_p c_2 \left(1 - R(d)^{B_{eff}/A_p W_p (2A_p W_p c_2 + c_1)} \right) e^{(c_1 - \sqrt{c_1^2 + 4c_2 \Delta p}) / (2A_p W_p c_2 + c_1)} + c_1 \right\}^2 - c_1^2 \right] \tag{17}$$

This equation fails to offer a closed form solution on account of the appearance of a pressure term in the natural exponent on the right hand side. Further investigation is thus needed to draw rigorous conclusions on the transient behaviour of the pressure differential. Two specific cases will be addressed here: purely laminar flow and purely turbulent flow. The former is convenient, as an exact solution can be found, while comparisons with the latter are included on account of the popularity of such models.

Considering laminar flow, if $c_2 = 0$ Eq. (17) becomes

$$\Delta p|_{c_2 = 0} = A_p W_p c_1 \left(1 - R(d)^{B_{eff}/A_p W_p c_1} \right) \tag{18}$$

This result shows that as $d \rightarrow 1$, causing $R(d) \rightarrow 0$, then $\Delta p \rightarrow A_p W_p c_1$. Thus, as the piston approaches the end of the cylinder and the volume in the chamber goes to zero, the pressure differential approaches its supposed equilibrium: the same value predicted using incompressible assumptions. The question remains as to the nature of its approach; the above equation does not in itself confirm the assumed asymptotic approach. Substituting $R(d)$ from (15) back to (18) and taking its first derivative with respect to time gives

$$\Delta \dot{p}|_{c_2 = 0} = B_{eff} A_p W_p \left(\frac{V_{0,1} + V_{0,2}}{V_{0,1} V_{0,2}} \right) \left(\frac{(1-d)^{G_1 - 1}}{(1 + (V_{0,1}/V_{0,2})d)^{G_1 + 1}} \right) \tag{19}$$

where $G_1 = B_{eff}/A_p W_p c_1$. From this equation the variation of the pressure is seen to be qualitatively dependent upon the value of G_1 . If $G_1 > 1$ then the numerator is zero when $d=1$ so the pressure differential between the chambers is static. If $G_1 < 1$ then $\Delta \dot{p} \rightarrow \infty$ as $d \rightarrow 1$. From this observation it can be concluded that a prerequisite for a converging pressure differential is that $G_1 > 1$. Furthermore, the greater the value of G_1 , the faster the numerator will converge to zero and the faster the pressure differential will converge to a steady state. Thus a fast convergence is associated with a large bulk modulus (i.e. small compressibility), a small piston area, a low piston velocity, and a small linear loss coefficient. Fig. 2 illustrates the qualitative shape change in the pressure differential curve, followed by the faster convergence for increasing values of G_1 .

Turning attention to the more common turbulent orifice flow model, letting $c_1 = 0$ in Eq. (17) produces

$$\Delta p|_{c_1 = 0} = (A_p W_p)^2 c_2 \left(1 - R(d)^{B_{eff}/2(A_p W_p)^2 c_2} e^{-\sqrt{\Delta p/(A_p W_p)^2 c_2}} \right)^2 \tag{20}$$

which is no longer closed form. In other respects the solution is similar to that of Eq. (18). When the piston reaches the end of the cylinder and $d=1$, then $R(d)=0$ and the pressure differential once again takes on its incompressible value: $\Delta p = (A_p W_p)^2 c_2$. At this time $\Delta p/(A_p W_p)^2 c_2 = 1$ and the exponential expression gives $e^{-1} \approx 0.37$, while at time $t=0$ then $\Delta p/(A_p W_p)^2 c_2 = 0$ and $e^0 = 1$. The exponential term thus varies from 1 to 0.37 for positive pressure differentials, speeding up the convergence compared with the laminar flow case. The squaring of the right hand side, however, counters this effect and serves to slow the convergence. The time derivative of Eq. (20) is found to be

$$\Delta \dot{p}|_{c_1 = 0} = B_{eff} \sqrt{\frac{\Delta p}{c_2}} \left(\frac{V_{0,1} + V_{0,2}}{V_{0,1} V_{0,2}} \right) \left(\frac{(1-d)^{G_2 - 1}}{(1 + (V_{0,1}/V_{0,2})d)^{G_2 + 1}} \right) \left(e^{\sqrt{\Delta p/(A_p W_p)^2 c_2}} - R(d)^{G_2} \right)^{-1} \tag{21}$$

which exhibits a numerator of $(1-d)^{G_2 - 1}$, equivalent to that of the linear case, where now $G_2 = B_{eff}/2(A_p W_p)^2 c_2$. Once more the numerator will be infinite when $d=1$ if $G_2 < 1$, so a suitable convergence has a prerequisite of $G_2 > 1$. The pressure differential curves for a range of values of G_2 are shown in Fig. 2.

The general form of G for a serial laminar–turbulent arrangement can be given as

$$G_3 = \frac{B_{eff}}{2(A_p W_p)^2 c_2 + A_p W_p c_1} = \frac{B_{eff}}{A_p W_p c_3} \tag{22}$$

corresponding to a linear–quadratic pressure differential derivative of

$$\Delta \dot{p} = B_{eff} \varphi(\Delta p) \left(\frac{V_{0,1} + V_{0,2}}{V_{0,1} V_{0,2}} \right) \left(\frac{(1-d)^{G_3 - 1}}{(1 + (V_{0,1}/V_{0,2})d)^{G_3 + 1}} \right) \left(c_3 e^{\varphi(\Delta p) - c_1/c_3} - 2c_2 R(d)^{G_3} \right)^{-1} \tag{23}$$

where $c_3 = 2A_p W_p c_2 + c_1$ is a constant based upon the loss coefficients and piston geometry: in effect a mixed flow loss coefficient; and $\varphi(\Delta p) = (c_1^2 + 4c_2 \Delta p)^{1/2}$ is an adjusted measure of the pressure differential. It is also instructive to normalise the pressure differential term with respect to the incompressible value, and noting that $Q = A_p W_p$ for incompressible fluid, Eq. (7) gives

$$\Delta p|_{B_{eff} = \infty} = A_p W_p c_1 + (A_p W_p)^2 c_2 \tag{24}$$

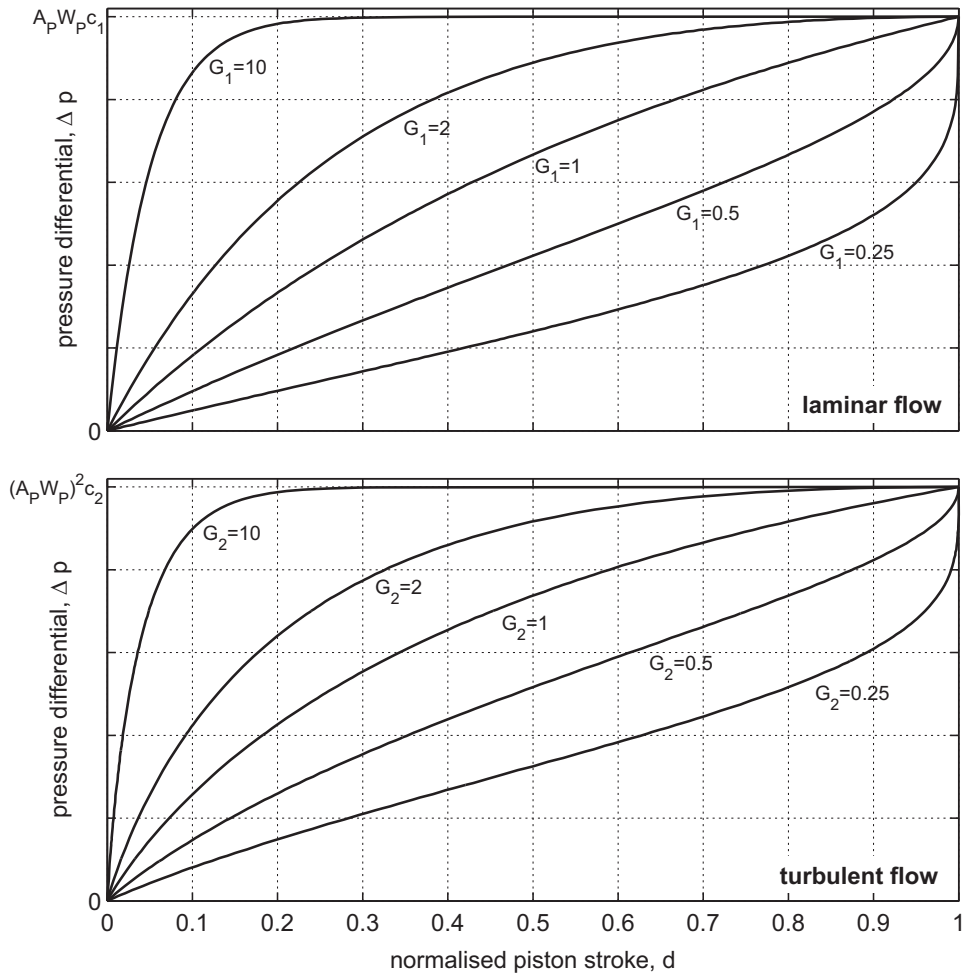


Fig. 2. Illustration of the different pressure differential convergence rates with laminar and quadratic orifice flows for increasing G_1 and G_2 , respectively. A central starting position is assumed: $V_{0,1}/V_{0,2}=1.15$.

for positive W_p . Thus, a normalised quantity can be introduced so that $\phi = \Delta p / (\Delta p|_{B_{eff} = \infty})$ leading to the following formula for $\varphi(\Delta p)$:

$$\varphi(\Delta p) = ((1 - \phi)c_1^2 + \phi c_3^2)^{1/2} \tag{25}$$

It is interesting to note how the laminar terms dominate for small values of ϕ , where the pressure differential is low, and the mixed loss coefficient c_3 dominates when ϕ approaches unity.

The above equations demonstrate how the attainment of a quasi-steady state, comparable to incompressible flow conditions, is contingent primarily upon a high enough value of G_3 , defined by Eq. (22). How high is ‘high enough’ depends on the accuracy required for the study, and this will be considered in the test design discussions that follow.

3.3. Proposed experiment methodology and test design

The previously described configuration, with constant velocity excitation, is formalised in this section. To allow for repeatability checks during the test process, the input velocity signal to the system is assumed to be piecewise constant corresponding to the triangular piston displacement signal. A single excitation cycle can thus induce two opposite and nominally equal piston velocities allowing investigation of the directional effects in the damper. A controlled sequence of triangular signals with appropriately chosen parameters produces a range of piston velocities and corresponding flow conditions. A choice of excitation signal parameters which provide varying density may be desirable to provide a complete picture about the performance of the damper, for example concentrating measurements in flow mode transitional regions, or in the neighbourhood of conditional activation of the valves.

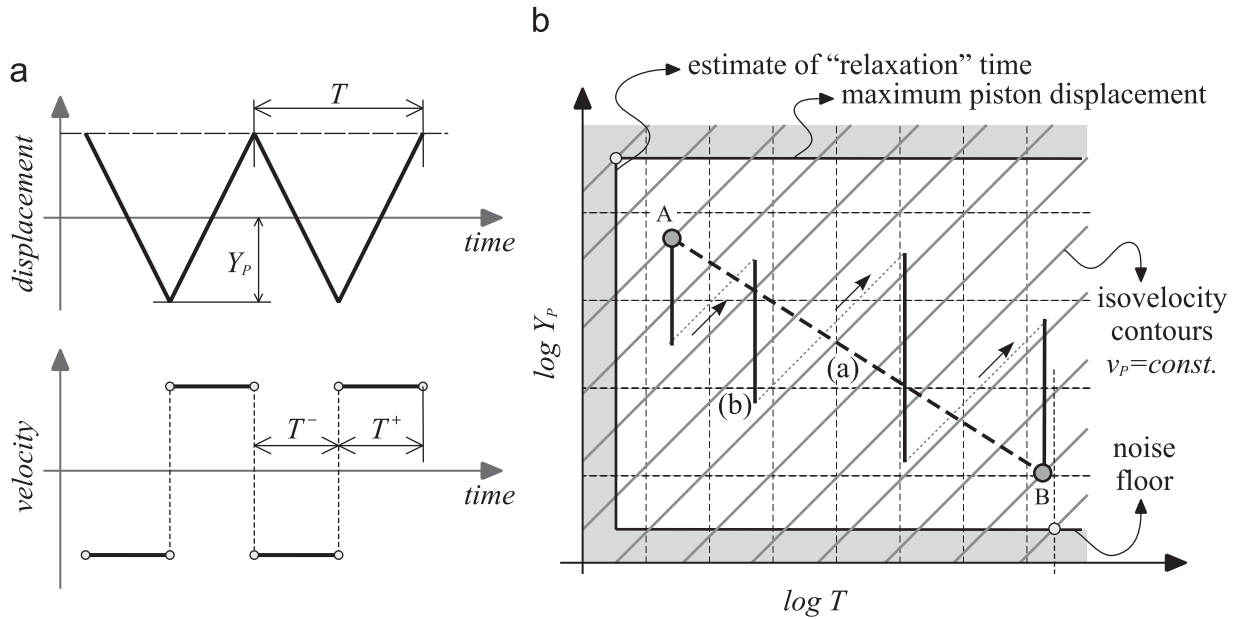


Fig. 3. Piecewise constant-velocity excitation for damper performance mapping: (a) triangular excitation signal and (b) A–T diagram for the test design.

A triangular piston excitation around the reference piston position is assumed in the following form:

$$y_p(t) = Y_p \text{tri}(\Omega t + \varphi_p),$$

$$\dot{y}_p(t) = \mathcal{E}(t) 2\Omega Y_p / \pi = \mathcal{E}(t) 4Y_p / T = \mathcal{E}(t) W_p, \quad \mathcal{E}(t) = \begin{cases} +1, & t \in T^+ \\ -1, & t \in T^- \end{cases} \quad (26)$$

where $\text{tri}(\cdot) \in [-1, +1]$ is the function generating the triangular signal, Ω is the angular frequency, Y_p is the amplitude of triangular waveform, φ_p is the phase of the waveform, and T^+ and T^- represent “half-periods” of the triangular signal with period T with positive and negative slopes, respectively. An example of this signal and its derivative is presented in Fig. 3(a).

The absolute piston velocity $W_p = |\dot{y}_p(t)| = 4Y_p/T$ is specified by means of two free parameters, the amplitude of triangular waveform Y_p and its period T . A choice of the two parameters is required to specify any given piston velocity, as illustrated in Fig. 3(b). This figure presents an amplitude–period design chart (henceforth an A–T diagram). Application of the logarithmic transformation to the formula for W_p defines an “iso-kinetic” plane with constant velocity contours

$$\log W_p = \log 4 + \log Y_p - \log T \quad (27)$$

This representation can be used to prepare the experimental conditions in the form of a sequence of the parameters $[\log T_i, \log Y_{p,i}]$ for N_V test points. This allows characterisation of the steady damper performance between two limiting velocity points A and B. A specific test design is represented in this domain as a path connecting points A and B. Two exemplary test designs are represented by the dashed line (a) and the solid line (b) connecting limiting points A and B in Fig. 3(b). Alternative paths can be considered to allow suitable test optimisation. Furthermore, different density of the path discretisation allows localised studies, e.g. relief valve activation velocity.

Some additional constraints have to be taken into consideration during actual test planning. The A–T diagram allows inclusion of some of these directly into the test plan. This is illustrated in Fig. 3(b) for the case of three constraints: (i) limited permissible piston travel, (ii) measurement noise floor due to piston displacement sensors, and (iii) minimum time required to achieve quasi-steady values of the measured forces. The first two constraints can be derived directly from inspection of the damper and sensors, while the third constraint can be based either on a conservative *a priori* estimate, or it can be derived *a posteriori* from the complete measured damper response records.

The method outlined above by-passes problems with mechanical backlash, significantly reduces “hysteretic” effects due to highly resistive hydraulic restrictors during harmonic excitation tests, and minimises the influence of the actuator dynamics. The constant velocity excitation effectively removes piston inertia effects and allows more focused investigations in the velocity regions of interest. The effect of directional flow dependencies can be investigated as well with this approach. Another important feature of this methodology is that it allows estimation of the overall damper characteristics. A negative aspect of this methodology is that, in a single test run, it provides only one pair of the experimental points, instead of whole groups or loops as is the case with alternative existing methodologies.

4. Case study

4.1. Test platform and test configuration

The previously described test methodology is applied in this section to the industrial hydraulic damper, used in medium-sized production helicopter rotors for stability augmentation [28]. The basic organisation of the damper test rig and a description of the damper's functional components is provided in Fig. 4. The damper test rig consists of the hydraulic damper attached to a bracket on one side and to a Hydrolups™ servohydraulic actuator on the other side. The mechanical link between the damper and the actuator is formed by a 25 kN load cell augmented with a damper attachment fixture. The organisation of the test rig is illustrated in Fig. 4(a). The test rig is controlled with the help of two computers and the Instron Structural Testing system Labtronic 8800 with a standard PID-based controller, in displacement control mode. The first computer is simply a user interface for the Labtronic 8800, which is controlled via an auxiliary control signal. This signal is provided by a dSpace DS1103 system attached to the second computer, equipped with the Matlab-Simulink programming platform and dSpace ControlDesk suite.

Purpose built Matlab-Simulink test control software was compiled and during the experiment exported to the real-time environment of the dSpace DS1103. This test control software provides control of the experiment according to the A–T diagram (Fig. 3(b)). One of the tasks covered by this platform is generation of the demanded actuator displacement signal $y_{p,command}$. Observed quantities are: the actuator piston displacement $y_{p,meas}$, measured by the LVDT transducer integrated with the actuator, and the force F_D measured by the load cell. The signals $y_{p,meas}$ and F_D are further processed as described later in this paper.

The damper internal organisation is shown in Fig. 4(b). The device is a hydraulic damper with a symmetric piston and an orifice located in the piston head. The orifice forms the primary flow path and it defines the low-velocity pressure-flow regime characterised by a steep rise of damper forces with increasing velocity. The rise of the forces is restricted by a pair of relief valves. The relief valves and their respective flow paths are denoted by the grey lines in Fig. 4(b). The components described so far represent the damper's functional parts, these being primarily responsible for its operational characteristics. A second part of the damper, consisting of a fluid accumulator and its flow network, is not shown in Fig. 4(b) as it does not significantly influence the damper behaviour. Further information on the operational context of this damper can be found in [28].

The current study investigates the low-velocity characteristics of the damper that are nominally defined by the single piston orifice. A practical motivation behind this study is the highly resistive nature of this orifice, which causes strong interaction between the “hysteretic” compressibility effects and the static characteristics during traditional tests with harmonic excitation signals. A further complication with these traditional tests is introduced by the appearance of mechanical backlash. It is assumed that during the current investigations both relief valves stay nominally closed. The purpose of this study is to identify and evaluate the qualitative nature of the overall losses induced in the damper's low-velocity range and to compare these with the losses determined from the nominal parametric model of the damper in this regime.

4.2. A study of transient effects in the damper

For the approach being taken, a critical consideration is how much time to allow for the transient force, or pressure differential, characteristics to subside. This was seen as one of the constraints illustrated in Fig. 3(b). In Section 3.2 it was seen that true steady-state conditions are never achieved. To quantify the speed of convergence towards quasi-steady conditions, where the pressure differential is close to the equivalent incompressible value, it is helpful to plot the piston stroke required to achieve a given normalised pressure differential (derived in Section 3.2). Rearranging Eq. (17) gives

$$d = \frac{1 - \left\{ \left(\frac{c_3 - \varphi}{2A_p W_p c_2} \right) e^{(\varphi - c_1)/c_3} \right\}^{1/G_3}}{1 + \left(\frac{V_{0,1}}{V_{0,2}} \right) \left\{ \left(\frac{c_3 - \varphi}{2A_p W_p c_2} \right) e^{(\varphi - c_1)/c_3} \right\}^{1/G_3}} \quad (28)$$

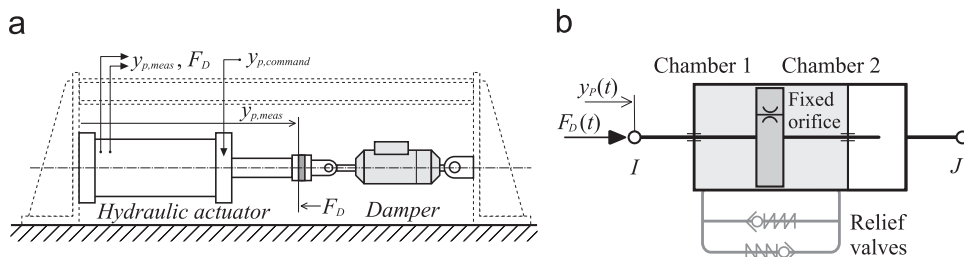


Fig. 4. Functional organisation of the test rig and the internal structure of the damper.

Table 1
Geometric parameters measured from physical damper and assumed fluid properties.

Quantity	Value	Quantity	Value
Piston area, A_p	$\sim 4 \times 10^{-3} \text{ m}^2$	Orifice area, A_o	$\sim 6 \times 10^{-8} \text{ m}^2$
Initial volume of each chamber, $V_{o,1}=V_{o,2}$	$\sim 3 \times 10^{-4} \text{ m}^3$	Orifice pipe length, l_o	$\sim 5 \times 10^{-4} \text{ m}$
Oil compressibility, β_{oil}	$3.8 \times 10^{-9} \text{ Pa}^{-1}$	Lin. orifice coeff., c_1	$8\pi l_o \mu / A_o^2$
Oil density, ρ	815 kg/m^3	Quad. orifice coeff., c_2	$\rho / (2A_o^2 C_D^2)$
Oil viscosity, μ	0.03 kg/(m s)	Air compressibility (isothermal), $\beta_{air} \equiv \beta_G$	$9.9 \times 10^{-6} \text{ Pa}^{-1}$
Discharge coeff., C_D	0.6 (dimensionless)		

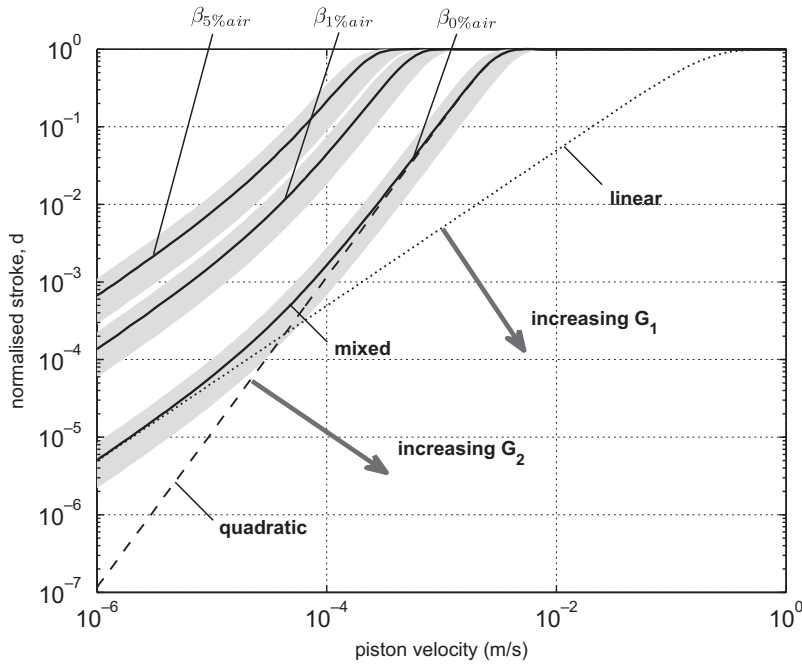


Fig. 5. Piston stroke required to achieve 99.9% of the incompressible pressure differential for various piston velocities, assuming linear (laminar), quadratic (turbulent), or mixed linear–quadratic flow, the latter shown with varying amounts of air contamination in the hydraulic oil.

and together with Eq. (25) it permits the determination of the normalised piston stroke required to attain a given fraction, ϕ , of the incompressible pressure differential. The laminar and quadratic cases are presented below for comparison:

$$d \Big|_{c_2=0} = \frac{1-(1-\phi)^{1/G_1}}{1+(V_{o,1}/V_{o,2})(1-\phi)^{1/G_1}}, \quad d \Big|_{c_1=0} = \frac{1-\{(1-\sqrt{\phi})e^{\sqrt{\phi}}\}^{1/G_1}}{1+(V_{o,1}/V_{o,2})\{(1-\sqrt{\phi})e^{\sqrt{\phi}}\}^{1/G_1}} \tag{29}$$

In the linear, laminar flow case, the normalised relationship between pressure and stroke is governed entirely by the quantity $G_1 \equiv G_3$, and the normalised starting position of the piston, $V_{o,1}/V_{o,2}$. In the turbulent case, the pressure–stroke relationship depends on $G_2 \equiv G_3$. To compare the laminar and turbulent cases it is necessary to define the damper geometry and test conditions relating G_1 to G_2 . To this end, measured geometric data from the real damper is used to produce the figures that follow, assuming a constant damper geometry and varying piston speeds. The damper geometries and orifice loss coefficients are given in Table 1 along with the working fluid properties.

Assuming a central starting position, Fig. 5 shows the relationship between the laminar, turbulent and combined flow cases, as well as demonstrating the effect of different effective fluid compressibilities, β_{eff} , on the mixed flow convergence times. The change in compressibility is effected in this case by the inclusion of small quantities of air mixed with the hydraulic oil. The shaded regions in the figure denote 95.0–99.999% of the incompressible pressure differential for the serial laminar–turbulent flow cases. The area to the left of the curves represents the design space available for the test configuration. If higher accuracies are demanded in the estimation of the steady state pressure differential, the design space is reduced. Generally the limiting factor will be the available piston travel, and an important observation is that air contamination in the oil produces significant reductions in the range of velocities that can be tested with a given piston stroke and a specified pressure convergence criterion. This contingency must be accounted for in the preparation of the test

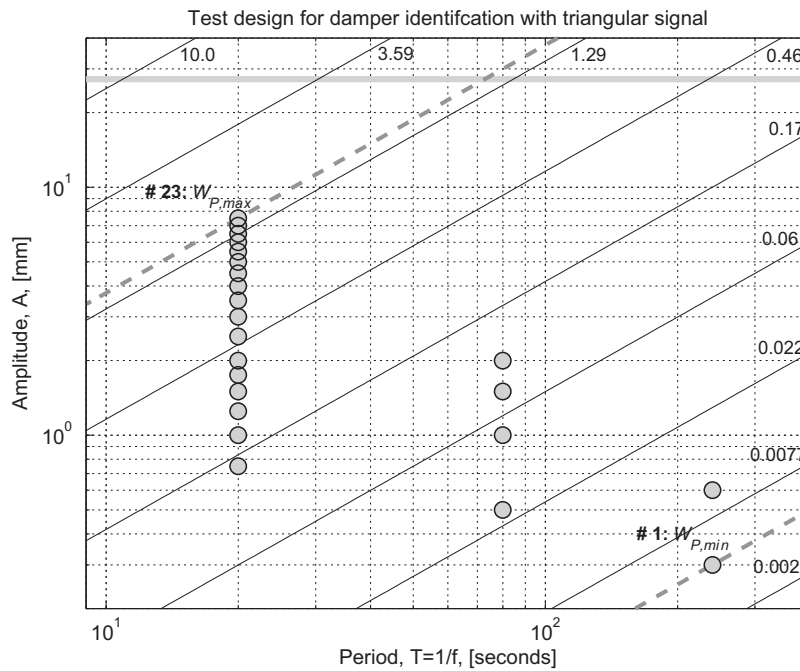


Fig. 6. A–T diagram for mapping of the steady damper performance.

configuration. For larger values of G_1 and G_2 (i.e. for lower loss coefficients) the design space is less restrictive, but the most restrictive coefficient will always dominate.

4.3. Test plan with A–T diagram

The A–T diagram with the selected test velocities is shown in Fig. 6. The range of velocities is selected to cover the majority of the low-velocity range. The information corresponding to the relief valve activation thresholds (characteristic piston velocity and activation force levels) are not presented here as they are not publically available.

The test plan is designed for the range of velocities $W_{p,i} \in [0.005, 1.5]$ mm/s, where $i = 1, \dots, 23$. This range of test velocities is chosen to provide a good understanding of the transition between the different flow modes. Furthermore, a pair of extremely low velocities is selected to give an indication of the friction effects. The specific parameter pairs selected to define the triangular waveforms, $[\log T_i, \log Y_{p,i}]$, are illustrated in Fig. 6 in the form of circle markers. Three groups of triangular signals are specified on the basis of their periods $T \in \{20, 80, 240\}$ s. This arrangement was adopted in order to reduce test times for separate test cases, while avoiding very low amplitudes, respecting the maximum allowed piston travel, and facilitating an automated acquisition process through consistent data acquisition times within each group.

The surface temperature of the damper during the tests was approximately 40 °C. The phase angle of the signal in Eq. (26) is defined for all test cases as $\phi_p = -\pi/2$ and the length of data acquisition is $2 \times T$, where T is the signal's fundamental period. This test signal specification provides two complete consecutive measurements for the two opposite flow directions.

4.4. Primary test processing

An important part of the test procedure is the processing of the raw experimental data in the form of the measured piston displacements and damper forces. The purpose of this operation is the extraction of the data subsets with stabilised or quasi-steady forces. Three selected test cases are provided in Fig. 7.

Test cases 4, 12 and 22 are shown in the time domain in the left column of Fig. 7, while the standard representation in the displacement–force domain is shown in the right column of Fig. 7. All the quantities are scaled to achieve a comparable level of visual detail in the presented data. Test case 4 clearly demonstrates the increased presence of noise in the measured data due to the low absolute force levels, where $\tilde{F}_D^+ \approx 0.102$ kN and $\tilde{F}_D^- \approx -0.095$ kN. The displacement signal presented indicates very good linearity and the damper force achieves an apparently steady level after a brief transient period, as suggested following the discussion of the models in Section 2. Test case 12 demonstrates the decreasing effect of noise in the measured force data and similar qualitative features can be observed here as in the previous case. The absolute force levels are $\tilde{F}_D^+ \approx 0.802$ kN and $\tilde{F}_D^- \approx -0.812$ kN. Similar conclusions can be drawn for set 22, with absolute damper forces of $\tilde{F}_D^+ \approx 6.590$ kN and $\tilde{F}_D^- \approx -7.366$ kN.

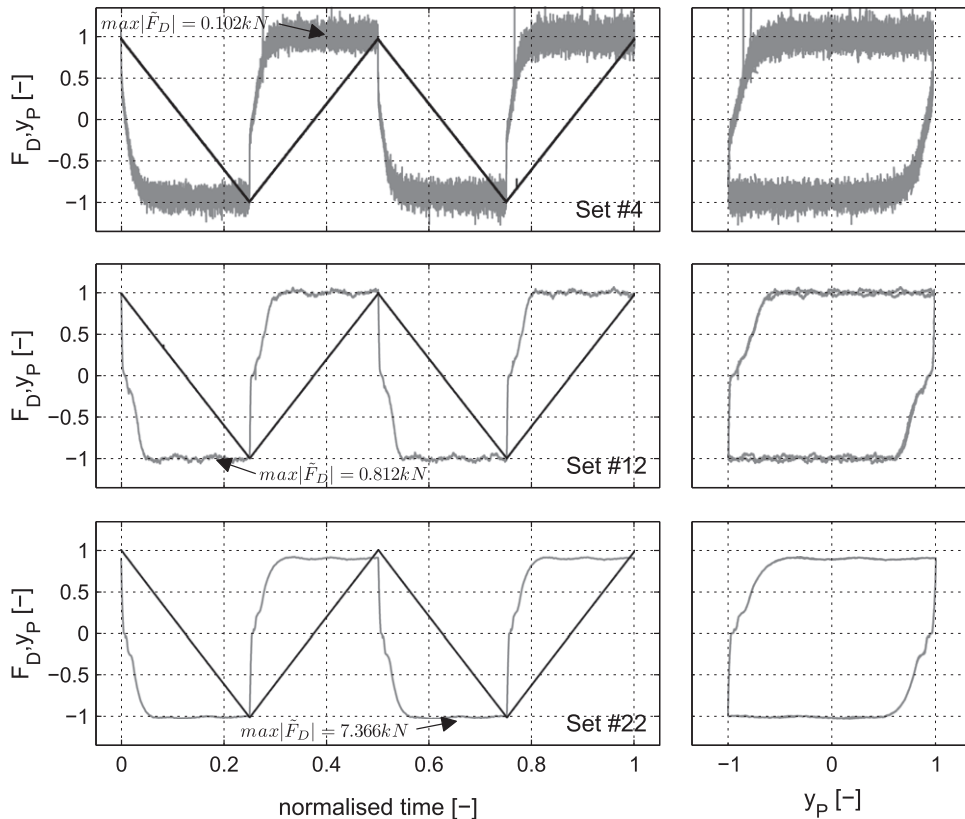


Fig. 7. Example of three selected test cases with triangular waveform excitation (scaling used to achieve consistent level of detail in the visual representation).

Even though the signals in Fig. 7 are scaled independently, it is still possible to observe some global effects in the form of the changing nature of the steady force asymmetries. For this purpose, the scaled piston displacement signal can be taken as a symmetric visual guide. Test case 4 indicated slightly higher positive forces levels $|\bar{F}_D^+|$ compared to the negative force levels $|\bar{F}_D^-|$. Conversely, in test case 22, negative force levels $|\bar{F}_D^-|$ are larger than the positive forces $|\bar{F}_D^+|$. These effects are caused by two different physical mechanisms. While test case 4 is influenced by friction, the dominant effects in test case 22 are of hydrodynamic origin, i.e. the pressure losses due to constricted fluid flow between the damper chambers.

Further presentation of the measured data and the applied data processing is shown in Fig. 8. The measured damper forces are shown with physical units and the measured piston displacements are plotted in a scaled form. The data subsets selected for the identification of the mean steady forces are indicated as solid black lines with dot markers. Similarly, the corresponding data subsets used for the experimental piston velocity identification are indicated as thick grey lines with dot markers. Finally, the variability of the force levels within the selected data subsets is represented by their standard deviation, and this value is visually identified by the solid line with the “+” markers. The data subsets are selected identically in all test cases as the data samples in the interval $[0.45, 0.95] \times T/2$, where $T/2 = T^+ = T^-$. This arrangement allows determination of the characteristics for both flow directions, thus evaluating any potential asymmetries. It also provides two independent curves for each direction, thus providing a tool to check for repeatability in the test results.

4.5. Test results and flow analysis for steady flow conditions

The results of all 23 test cases are summarised in Fig. 9. The curve presented represents the damper characteristics for the induced quasi-steady flow conditions at 40 °C (measured on the surface of the damper). The identified characteristics consist of two branches, located in the 1st and the 3rd quadrants of the velocity–force domain. Each test case is represented by a circle marker. The thick grey line in the background shows the same characteristics identified from the second period of the measured signals. The line may be hard to distinguish, as it lies almost exactly behind the first line.

As the test conditions cover a relatively wide range of forces, a detail of the extremely low velocity characteristics is provided in Fig. 10. This figure illustrates better the non-linear effects associated with decreasing piston speed. The following significant effects can be observed in the identified characteristics when $\dot{y}_p \rightarrow 0$: (a) the varying nature of the

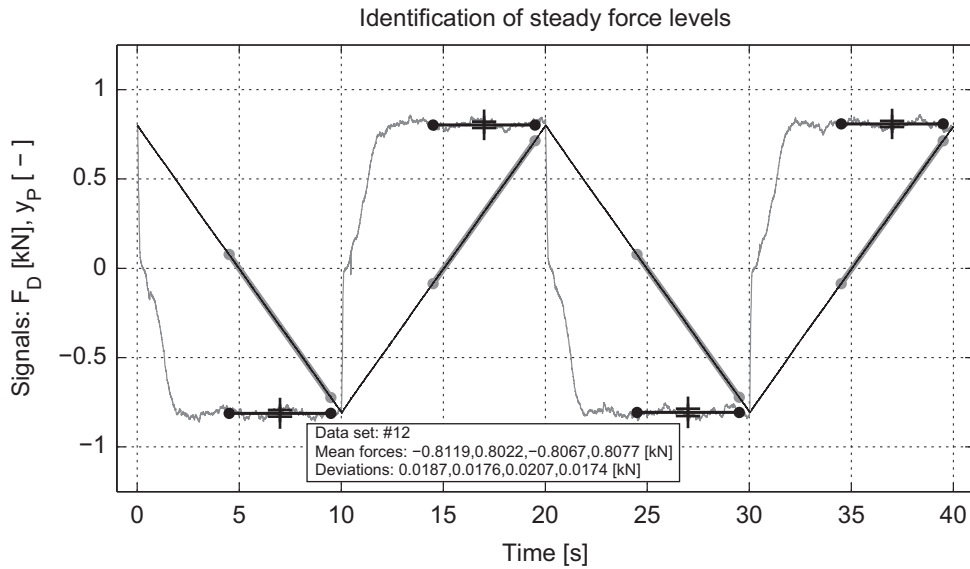


Fig. 8. Example of identification process of the steady force levels from the single test case.

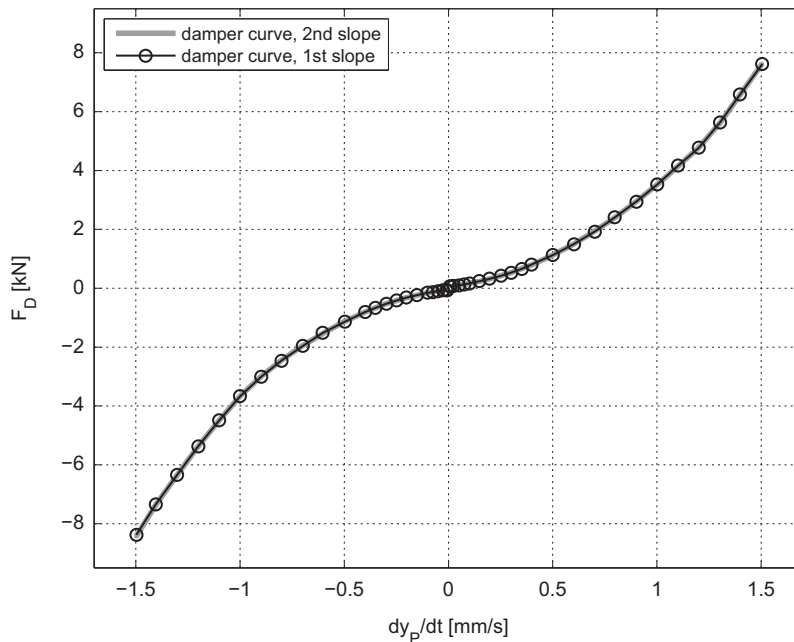


Fig. 9. Damper static characteristics determined from the tests with triangular displacement excitations.

fluid flow mode, (b) the convergence to non-zero force levels for both flow directions, (c) the asymmetric shape of the identified branches, and (d) close repeatability in the identified characteristics.

The previous observations can be correlated with an analytical model presented by Wallaschek [25] and later extended by Surace et al. [22]. The model presented in [25] is an analytical aggregate model combining the laminar–turbulent flow assumption in Eq. (7) with a simple Coulomb model of friction. This model is extended by using an assumption of asymmetric characteristics in [22], where two independent sets of parameters characterising laminar, turbulent and friction losses are considered for the opposite piston motions.

The changing nature of the fluid flow observable in Fig. 9 is more clearly seen in the logarithmic domain presented in Fig. 11. Non-zero damper forces for the piston velocities approaching zero can be related to the mechanical friction between the moving parts of the damper. Asymmetries in the shape of the characteristics for higher piston velocities can

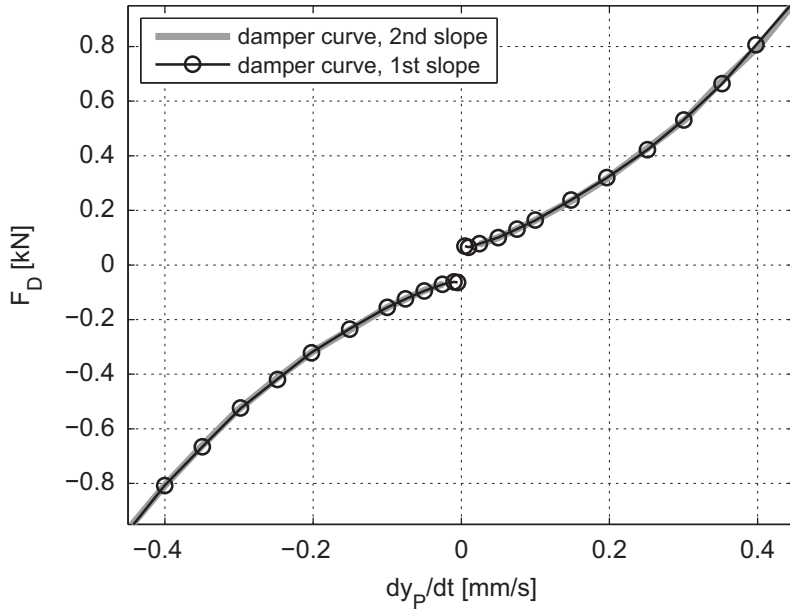


Fig. 10. Low velocity detail of the identified damper static characteristics.

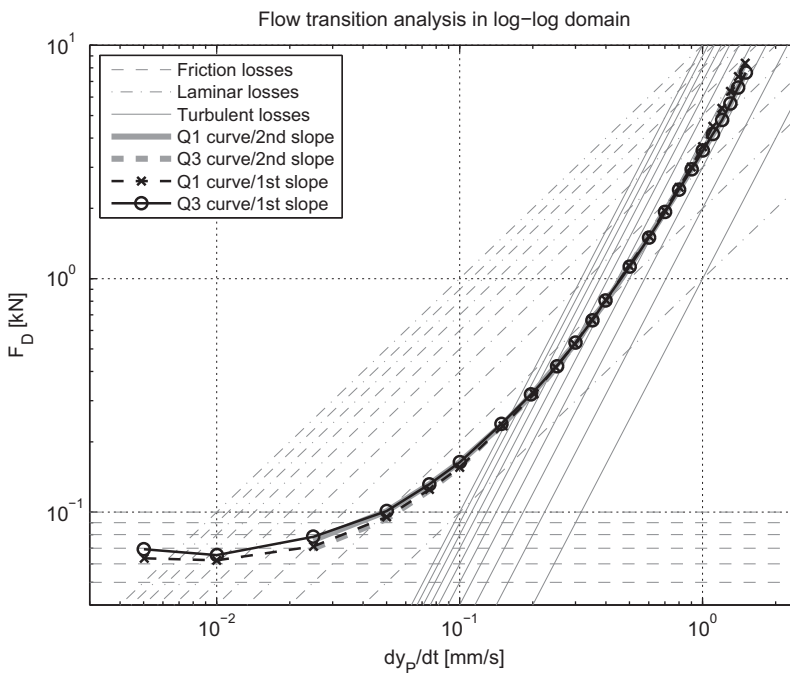


Fig. 11. Damper static characteristics represented in the logarithmic domain facilitating flow transition analysis.

be attributed to the asymmetric shape of the flow restricting paths between the working chambers of the damper. Consistent repeatability was observed in the measured data for all 23 data sets, offering confidence in the measured characteristics. Finally, the identified damper characteristics presented in Fig. 9 and detailed in Fig. 10 suggest, after neglecting friction effects, the presence and dominance of the laminar pressure losses for low piston velocities. These can be recognised by non-zero gradients at the origin.

To allow improved analysis of the flow mode transition, the characteristics shown in Fig. 11 can be related to the other single-term polynomial models based on the general formulation in Eq. (5). Families of curves can be considered for specific exponential terms and these can be related to discernible physical effects. Based on remarks presented in Section 2.2 and

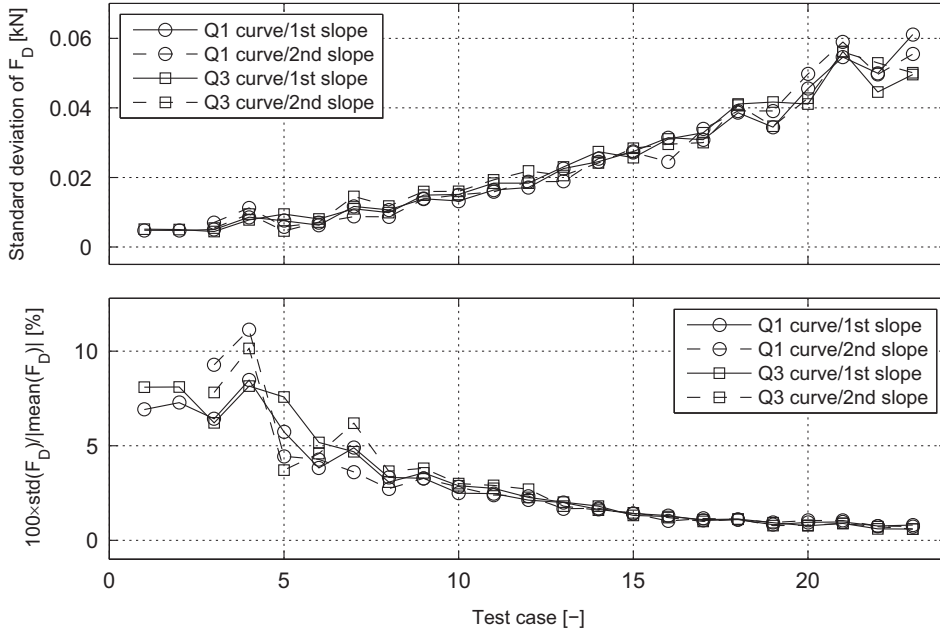


Fig. 12. Unsteady effects and noise identified in the steady regions of all test cases.

other findings presented in this section, the models considered here will include $\alpha \in \{0, 1, 2\}$. After applying the logarithmic coordinate transformation in Fig. 11, all families of exponential curves are converted to families of parallel skewed lines. Thus, in this system, any slope changes in the original identified curves can be associated with specific flow modes or physical mechanisms. The data from quadrant 3 are transformed to quadrant 1 for comparative purposes, by taking absolute values of their velocity and force coordinates.

The curves corresponding to the identified data from quadrant 1 are identified with circle markers and a thick solid line, while the data from the quadrant 3 are identified with star markers and a thick dashed line. The three families of exponential models are represented by the thin lines with styles according to the figure's legend. A transition in the character of the flow with increasing piston velocities is clearly indicated in this figure, corresponding with an increasing orifice flow Reynolds number. Two limiting regimes are represented by the friction at low piston velocities and the dominant turbulent flow at “high” piston velocities. These two physical modes can be visually inspected by looking at the convergence of the identified curves to the line families with $\alpha=0$ and 2. A section of the characteristics starting at approximately 0.5 mm/s can be related to the pressure-flow models based on the Blasius formula [4,26], and the models with free exponential parameters [5]. Increasingly turbulent fluid flow can be related to the line family with $\alpha=2$.

While Figs. 9 and 11 represent the characteristic damper curves alone, Fig. 12 complements these figures with information on the extent of the variability in the selected data subsets. The top subplot of this figure shows the absolute values of the standard deviations of the measured data. This subplot indicates that the variability in the steady responses increases with increasing piston excitation velocity, possibly being caused by unaccounted-for unsteady pressure fluctuations in the damper.

To give a better appreciation of the significance of these effects, the lower subplot of Fig. 12 shows the ratio between the standard deviations and the mean force values. Increased levels of variability (5–10%) are present in the regions influenced by friction, due to low steady force levels. The relative sizes of the deviations decrease to approximately 1% with increasing test number. Both subplots of this figure contain four lines, where each line corresponds to one segment of the test signal with constant slope. The similarity of the two pairs of lines (one for each quadrant) is indicative of good test repeatability.

The foregoing figures allow detailed non-parametric analysis of the damper and the steady state specifics of its performance. The identified damper characteristics shown in Fig. 9 are considered now in the wider context of alternative test methodologies and nominal model-based predictions. The parametric model of the damper is based on Eq. (9). Assuming the internal damper structure shown in Fig. 4(b) and pressure-flow model (7) with parameters c_1 and c_2 as defined in Section 2.2, the following simplified model of the damper's new hydraulic state $F_{D,h}$ can be written

$$\beta_{eff} \nu(t) \dot{F}_{D,h} + \text{sign}(F_{D,h}) A_p (-c_1 + \sqrt{c_1^2 + 4A_p^{-1} c_2 |F_{D,h}|}) / (2c_2) = A_p^2 \dot{y}_p \quad (30)$$

The assumption of an incompressible damper configuration, $\beta_{eff}=0$, in Eq. (30) and the subsequent rearrangement of the resulting algebraic equation leads to an explicit formula for the hydraulic component of the damper force:

$$F_{D,h} = D_L \dot{y}_p + D_Q \dot{y}_p |\dot{y}_p| = A_p^2 c_1 \dot{y}_p + A_p^3 c_2 \dot{y}_p |\dot{y}_p| \quad (31)$$

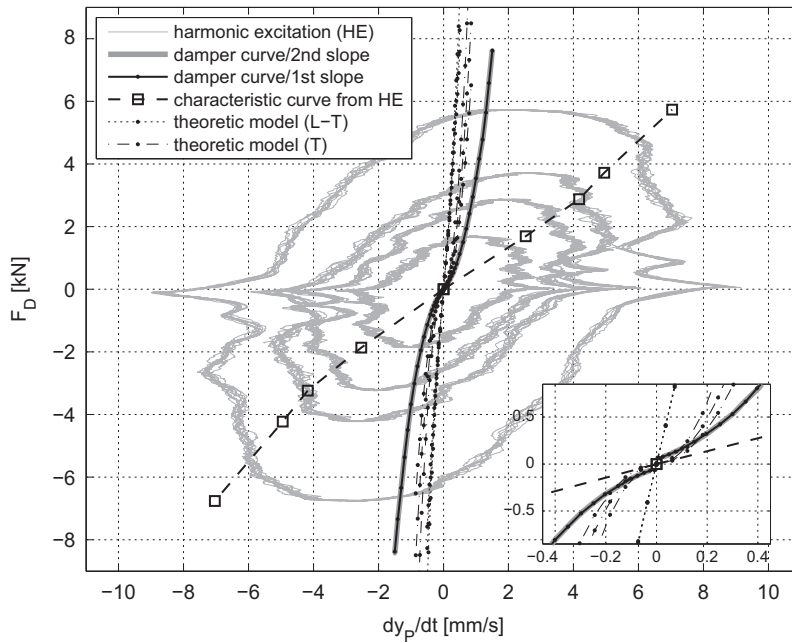


Fig. 13. Comparison of different damper characteristics.

Finally, assuming the specific parametric forms given in Section 2.2 for the flow coefficients c_1 and c_2 , the formula for $F_{D,h}$ is specified as follows:

$$F_{D,h} = 8\pi\mu_{40}l_0 \left(\frac{A_p^2}{A_0^2} \right) \dot{y}_p + \frac{\rho_{40}}{2C_D^2} \left(\frac{A_p^3}{A_0^2} \right) \dot{y}_p |\dot{y}_p| \quad (32)$$

where μ_{40} and $\rho_{40} \approx \rho$ are the dynamic viscosity and the fluid density at 40 °C, respectively. The other quantities in Eq. (32) are defined in the previous sections. The parameter values that are used in this formula are taken from Table 1. These parameters are either directly measured or adopted from available engineering sources. The model in Eqs. (31) and (32) represents a fully symmetric damper model. While the experimental data indicate considerable asymmetries, this model is used only for demonstration purposes and the qualitative comparisons provided in Figs. 13 and 14. Parametric identification based on the presented data could use two instances of the above model, each representing one direction of the piston motion. This approach is also physically justifiable due to the asymmetric design of the orifice primarily responsible for the observed pressure losses. The curves resulting from the use of Eq. (32) will be presented for three different values of the discharge coefficient $C_D \in \{0.6, 0.7, 0.8\}$, due to this parameter's uncertainty and its high dependency on the specific orifice context.

Fig. 13 summarises the results of two different experimental techniques and one analytical study. Results of the experiments with triangular piston excitation, originally presented in Figs. 9 and 10, are denoted in the legend of this figure as the “damper curves”. The results from the experiment with harmonic piston excitation, denoted as HE, are presented in the figure in the form of the “hysteretic” loops. The four different test cases are presented with the sine frequency 1.75 Hz and the amplitudes $\{0.23, 0.38, 0.45, 0.64\}$ mm. Additionally, an alternative representation of these loops is used in the form of the characteristic “peak-to-peak” curves. These curves can be seen as the summary test information from the harmonic tests and they consist of points representing the non-coincident extremes, or peaks in the velocities and forces for each harmonic excitation test case. The figure also contains two families of lines based on formula (32) denoted as the “theoretic model”. The first family assumes a purely turbulent flow mode and it is denoted by “T”. The second family assumes combined laminar–turbulent pressure losses and it is denoted by “L–T”. The three lines in each family correspond to the three discharge coefficients.

A number of qualitative and quantitative observations can be made in relation to the testing techniques and damper performance on the basis of Fig. 13. The results produced during the harmonic piston excitation tests, i.e. the “characteristic curve”, represent the lower boundary among the three data sets presented. This is due to the dynamic behaviour of the damper during the tests with variable piston velocities. This dynamic behaviour can be associated with the fluid–gas compressibility and it results in counter-clockwise loops in the measured data [9]. The sense of the rotation of these loops can be visually identified by looking at the positions of the velocity spikes corresponding to the mechanical backlash during zero damper force crossing. The smaller transients detectable in these loops, located after the initial, large

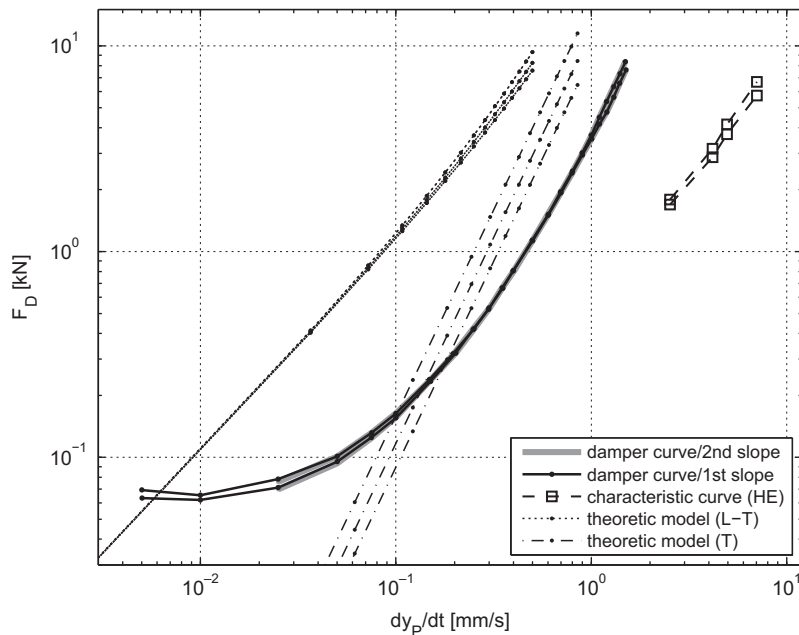


Fig. 14. Comparison of different damper characteristics in the logarithmic domain.

backlash spikes, indicate the counter-clockwise orientation of the loops. Overall, the damper appears to behave as “softer” than the one identified using the triangular piston excitation. In addition, the characteristic curve presented in the figure is specific to the applied harmonic excitation frequency. In this respect, the tests with constant piston velocity can be seen as harmonic tests with an infinitely long period, or infinitesimal frequency.

The perceived upper boundary in the characteristics shown in Fig. 13 is associated with the parametric predictions computed from model (32). Both families of these curves are characterised by a steeper rise than the curves identified from the triangular piston excitation tests. This rise is indicative of the lower pressure losses in the actual physical damper setup. The parametric predictions of the damper forces are calculated based on the best attainable information about the relevant geometries and properties, so the results shown in the figure suggest the possibility of additional unmodeled flow paths. One candidate for a previously unidentified flow path is the leakage flow between the piston and the damper cylinder walls.

The foregoing analysis points to the usefulness of the testing procedure presented here. The two primary applications of this approach include: (a) damper model refinement via the qualitative and quantitative analysis of the identified velocity–force characteristics and (b) semi-empirical representation of the overall pressure–flow characteristics derived from the identified velocity–force characteristics for further use in model (1). Some other alternative applications of this methodology can be friction identification, overall damper asymmetry evaluation or quality and performance monitoring.

The analysis in this section is concluded with Fig. 14, which complements Fig. 13. The identified results are presented here in the logarithmic coordinate system allowing further evaluation of the nature of the flows modes and their transitions. The identified results from the third quadrant are in this case again projected to the first quadrant to allow logarithmic transformation.

Fig. 14 complements earlier observations by indicating the insufficiency of the parametric predictions, using nominal parameter values, in capturing the actual loss mechanism. This deficiency is apparent in the different slopes and the offset of the measured characteristics, showing significant over-predictions in the actual steady forces. However, as expected the predicted turbulent and identified damper curves tend to share similar slopes for higher piston velocities.

5. Conclusions

This paper provides a detailed exposition of a valuable test methodology in the analysis of hydraulic dampers. The technique uses triangular displacement signals applied to the damper piston to produce piecewise constant velocity excitation. This approach has been shown to allow robust automated identification of the steady state damper characteristics. It has been demonstrated that the resulting velocity–force curves can provide a useful tool in a variety of damper analysis tasks, including model validation, model refinement and quality and performance monitoring.

The paper focuses in particular on two aspects of the method: firstly, it provides an in-depth examination of the feasibility of the technique in the presence of transient pressure variations. Secondly, it presents a thorough demonstration on an industrially relevant device, and compares the results with those of analytical and traditional experimental methods.

The transient pressure variations occur with step changes in the excitation velocities, and hamper the identification of steady state characteristics. They are caused by effective compressibility of the working fluid, accounting for both the actual fluid compressibility and the related effects such as structural damper flexibilities and air contamination. It has been shown analytically that the resulting damper model responses are unsteady to some extent throughout the entire stroke of the piston. The conditions under which the responses approximate steady states have been investigated for laminar, turbulent and combined laminar–turbulent flows, and quantitative methods for determining suitable test regimes have been presented. Parametric studies found that for reasonable test configurations the response showed fast progression towards steady flow conditions, endorsing the application of the methodology to the identification of steady state characteristics.

The methodology was then tested on a lag damper: a device used in production helicopters for stability purposes. Specifically, the low-velocity operational regime of the damper was investigated to highlight the challenges posed by the use of hydraulic components with high loss coefficients. The validity of the results produced by this methodology was confirmed through their physical consistency with other predicted and measured results. In particular, the results from the proposed technique have been shown to have a direct physical relationship with the results of the traditional harmonic excitation tests. A comparison of the new results with the fully parametric model predictions, based on the nominal parameters and measured internal damper topology, suggests the need for augmentation of the damper model flow paths, incorporating for example cross-piston leakage through the seals. This observation typifies the insight offered by the rich and accessible results set produced with the methodology of this paper, and the formal framework presented here is intended to aid with the design of such tests.

Acknowledgements

The authors gratefully acknowledge the support of AgustaWestland. The authors also acknowledge useful discussions with Mr. Djamel Rezgui regarding the theoretical analysis.

References

- [1] L. Segel, H.H. Lang, The mechanics of automotive hydraulic dampers at high stroking frequencies, *Vehicle System Dynamics* 10 (2 & 3) (1981) 82–85.
- [2] M.D. Symans, M.C. Constantinou, Experimental testing and analytical modelling of semi-active fluid dampers for seismic protection, *Journal of Intelligent Material Systems and Structures* 8 (8) (1997) 644–657.
- [3] W.N. Patten, C. Mo, J. Kuehn, J. Lee, A primer on design of semiactive vibration absorbers (SAVA), *Journal of Engineering Mechanics* 124 (1) (1998) 61–68.
- [4] S.W.R. Duym, Simulation tools, modelling and identification, for an automotive shock absorber in the context of vehicle dynamics, *Vehicle System Dynamics* 33 (4) (2000) 261–285.
- [5] V.Y.B. Yung, D.J. Cole, Modelling high frequency force behaviour of hydraulic automotive dampers, *Vehicle System Dynamics* 44 (1) (2006) 1–31.
- [6] H.E. Merritt, in: *Hydraulic Control Systems*, John Wiley & Sons, New York, 1967.
- [7] Y. Jinghong, C. Zhaoneng, L. Yuanzhang, The variation of oil effective bulk modulus with pressure in hydraulic systems, *Journal of Dynamic Systems, Measurement, and Control* 116 (1) (1994) 146–150.
- [8] N.D. Manring, The effective fluid bulk-modulus within a hydrostatic transmission, *Journal of Dynamic Systems, Measurement, and Control* 119 (3) (1997) 462–466.
- [9] A.L. Audenino, G. Belingardi, Modelling the dynamic behaviour of a motorcycle damper, *Proceedings of the Institution of Mechanical Engineers, Part D, Journal of Automobile Engineering* 209 (4) (1995) 249–262.
- [10] A.H. Mitchell, K.L. Johnson, Simulation of a hydraulic actuator, *IBM Journal of Research and Development* 8 (3) (1964) 329–334.
- [11] A. Cardona, M. Gérardin, Modeling of a hydraulic actuator in flexible machine dynamics simulation, *Mechanism and Machine Theory* 25 (2) (1990) 193–207.
- [12] J.C. Ramos, A. Rivas, J. Biera, G. Sacramento, J.A. Sala, Development of a thermal model for automotive twin-tube shock absorbers, *Applied Thermal Engineering* 25 (11–12) (2005) 1836–1853.
- [13] P. Masarati, G.L. Ghiringhelli, M. Lanz, P. Mantegazza, Integration of hydraulic components in a multibody framework for rotorcraft analysis, in: 26th European Rotorcraft Forum, The Hague, The Netherlands, 26–29 September 2000, pp. 57.1–57.10.
- [14] J.C. Samin, O. Brüls, J.F. Collard, L. Sass, P. Fiset, Multiphysics modeling and optimization of mechatronic multibody systems, *Multibody System Dynamics* 18 (3) (2007) 345–373.
- [15] G.F. Davidson, Experiments on the flow of viscous fluids through orifices, *Proceedings of the Royal Society of London, Series A* 89 (608) (1913) 91–99.
- [16] G.L. Tuve, R.E. Sprengle, Orifice discharge coefficients for viscous liquids, *Instruments* 6 (1933) 201–206.
- [17] M. Borghi, G. Cantore, M. Milani, R. Paoluzzi, Analysis of hydraulic components using computational fluid dynamics models, *Proceedings of the Institution of Mechanical Engineers, Part C, Journal of Mechanical Engineering Science* 212 (7) (1998) 619–629.
- [18] J.A. Ferreira, F. Gomes de Almeida, M.R. Quintas, Semi-empirical model for a hydraulic servo-solenoid valve, *Proceedings of the Institution of Mechanical Engineers, Part I: Journal of Systems and Control Engineering* 216 (3) (2002) 237–248.
- [19] S. Hayashi, T. Hayase, T. Kurahashi, Chaos in a hydraulic control valve, *Journal of Fluids and Structures* 11 (6) (1997) 693–716.
- [20] R. Basso, Experimental characterisation of damping force in shock absorbers with constant velocity excitation, *Vehicle System Dynamics* 30 (6) (1998) 431–442.
- [21] R. Basso, G. Fanti, A technique for damping identification in shock absorbers, in: *Proceedings of the 1st International Conference: Integrating Dynamics, Condition Monitoring and Control for the 21st Century*, Manchester, UK, 1–3 September, 1999, pp. 15–20.
- [22] C. Surace, K. Worden, G.R. Tomlinson, On the non-linear characteristics of automotive shock absorbers, *Proceedings of the Institution of Mechanical Engineers, Part D, Journal of Automobile Engineering* 206 (1) (1992) 3–16.
- [23] B. Titurus, N. Lieven, Model validation and experimentally driven hydraulic damper model refinement, in: *ISMA2008 International Conference on Noise and Vibration Engineering*, September 15–17, 2008.

- [24] B. Titurus, N. Lieven, Modeling and analysis of semi-active damper in periodic working environments, *AIAA Journal* 47 (10) (2009) 2404–2416.
- [25] J. Wallaschek, Dynamics of non-linear automobile shock-absorbers, *International Journal of Non-Linear Mechanics* 25 (2–3) (1990) 299–308.
- [26] K. Reybrouck, A nonlinear parametric model of an automotive shock absorber, Society of Automotive Engineers, Paper 940869, March 1994, pp. 1170–1177.
- [27] W. Flügge, in: *Viscoelasticity*, 2nd revised ed., Springer-Verlag, Berlin, Heidelberg, 1975.
- [28] B. Titurus, N. Lieven, Integration of hydraulic lag-damper models with helicopter rotor simulations, *Journal of Guidance, Control, and Dynamics* 33 (1) (2010).